

Interpretable contour level selection for heat maps for gridded data

Tarn Duong*

23 May 2025

Abstract

Gridded data formats, where the observed multivariate data are aggregated into grid cells, ensure confidentiality and reduce storage requirements, with the trade-off that access to the underlying point data is lost. Heat maps are a highly pertinent visualisation for gridded data, and heat maps with a small number of well-selected contour levels offer improved interpretability over continuous contour levels. There are many possible contour level choices. Amongst them, density contour levels are highly suitable in many cases, and their probabilistic interpretation form a rigorous statistical basis for further quantitative data analyses. Current methods for computing density contour levels requires access to the observed point data, so they are not applicable to gridded data. To remedy this, we introduce an approximation of density contour levels for gridded data. We then compare our proposed method to existing contour level selection methods, and conclude that our proposal provides improved interpretability for synthetic and experimental gridded data.

Keywords: Highest density region, home range, hotspot, Jenks contour levels

1 Introduction

Gridded data are an effective format for the storage and dissemination of confidential and high-volume data. Confidential data are aggregated within a grid cell to ensure their privacy, whereas high volume data (aka Big data) are aggregated into grid cells to reduce their storage requirements. A heat map is a common visualisation method for bivariate gridded data where the value of the variable of interest is encoded by a colour scale. A continuous colour scale provides the most complete visualisation of the data (Tobler, 1973), though the large number of colours may impede interpretability (Jenks, 1963; Dobson, 1973). The usual approach to increasing interpretability is to reduce the number of distinct colours by assigning the same colour to an interval of values. The key question is to select an optimal set of contour levels and a colour scale to describe meaningfully the structure of the data surface (Klemelä, 2009). For simplicity, we treat the colour scale selection here as a secondary question, since we follow the recommendations in Zeileis et al. (2009), and focus our attention on the contour level selection.

There are many possibilities for the contour level selection: for example, the ‘natural’ contour levels (Jenks, 1967) are widely employed, especially for geospatial data. Despite their widespread acceptance, the spatial relevance of their associated contour regions has not been established rigorously within a statistical framework. In contrast, density contour levels rigorously define spatially relevant regions with a probabilistic interpretation which leads to highly interpretable visualisations (Bowman and Foster, 1993; Hyndman, 1996). A τ -density contour level is associated with the smallest region that contains τ probability mass of the data sample. For example, a contour region with a small τ (close to zero) is a data hotspot/cluster, e.g. for transportation data, this can be a traffic congestion or crash hotspot (Xie and Yan, 2008). The boundary of

*Paris, France F-75000. Email: tarn.duong@gmail.com. ORCID: 0000-0002-1198-3482.

the contour region of $\tau = 0.5$ can be considered to be a spatial median, since it divides the data sample where 50% of the data sample is inside and 50% is outside the contour boundary, e.g. for biomedical data, this is the characteristic territory of sub-cellular components in mammalian cells (Schauer et al., 2010). A contour region with a large τ (close to one) delimits most of the data domain, e.g. for zoological/botanical data, this is the home range for a biological organism (Baíllo and Chacón, 2021). The most popular method for calculating these density contour levels requires access to original point data which does not pertain to our case (Hyndman, 1996). Thus we propose an approximation of density contour levels which is suitable for gridded data.

Our first motivating data set is a 1×1 km gridded data set of socioeconomic indicators from the 2019 household census of about 30 million households in France, carried out by the French national statistical agency (Insee, 2019). The socioeconomic indicators involve income, poverty and housing etc. Due to their sensitive nature, this grid resolution is a trade-off between the dissemination of detailed socio-economic indicators for informed policy decision making, and the guarantee of privacy for individual households. We focus on the population density in the ROI (region of interest) is $[1.97^\circ\text{E}, 2.79^\circ\text{E}] \times [48.63^\circ\text{N}, 49.06^\circ\text{N}]$ which consists of 2078 grid cells and includes the Paris city centre and its inner ring of suburbs, as displayed in the left of Figure 1, in the EPSG 3035 projected coordinate system. The continuous colour scale, ranging from 40000 persons per km^2 (red) to 20000 persons per km^2 (orange) to 10000 persons per km^2 (yellow), provides a visually appealing heat map of the population distribution. We are able to identify qualitatively the densely populated regions (hotspots), though it is challenging to compute quantitatively these hotspots.

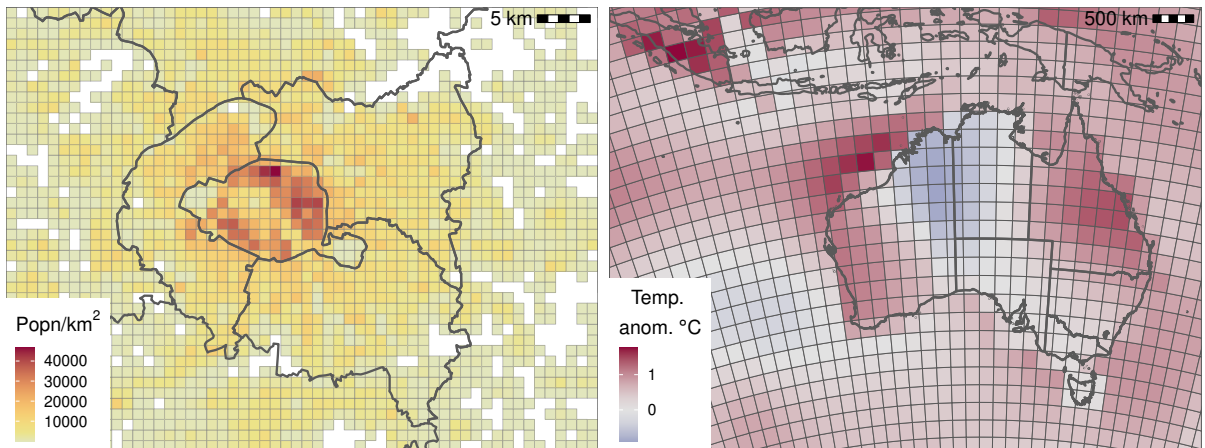


Figure 1: Heat maps for geospatial gridded data. (Left) Population of the Paris city region on 1×1 km grid, with continuous sequential colour scale. (Right) Surface temperature anomaly in the southern Indo-Pacific region on $2^\circ \times 2^\circ$ grid, with continuous diverging colour scale.

Our second motivating data set is the GISTEMP surface temperature anomalies on a $2^\circ \times 2^\circ$ grid (Lenssen et al., 2024; GISTEMP Team, 2025). The complete gridded data set covers all longitudes and latitudes, and for all months from 1880 to 2024. The temperature anomaly at each grid cell is the monthly mean temperature minus the long term mean temperature for the 20th century (1901–2000). It is a reconstructed data set, drawing from many high-volume point data sources, and the aggregation into grid cells is carried out to ensure comparable statistical reliability for all grid cells, so that it can serve as a global reference data source (Vose et al., 2021; Lenssen et al., 2024). We focus on the map for December 2020 in the ROI of the southern Indo-Pacific region, approximately covered by $[80^\circ\text{E}, 170^\circ\text{E}] \times [45^\circ\text{S}, 5^\circ\text{N}]$. We employ the EPSG 9473 projected coordinate system, so each $2^\circ \times 2^\circ$ square grid cell is transformed to variable curvilinear grid cells, as shown in the right of Figure 1. The temperature anomalies range from -0.89°C (blue) to 0°C (grey) to 1.76°C (red). The continuous colour scale poses fewer interpretative difficulties since there are fewer distinct colours than for the population data,

though it remains challenging to compute quantitatively the hot and cold spots.

Our third motivating data set is non-geospatial gridded data. It consists of the year, the month and the mean monthly GISTEMP temperature anomaly, for all years from 1880 to 2024, in the ROI $[111.28^\circ\text{E}, 129.43^\circ\text{E}] \times [35.79^\circ\text{S}, 12.68^\circ\text{S}]$ which covers the state of Western Australia. So it comprises 1740 grid cells for each year-month combination from 1880-01 to 2024-12. The heat map plots the year on the horizontal axis and the month on the vertical axis. The long term trends in Figure 2 is from cool anomalies (blue) in the first half of the year in the 1880–1900s to hot anomalies (red) in the second half of the year since the 2000s, though the visual impression of these trends is not overly strong due to the continuous colour scale.

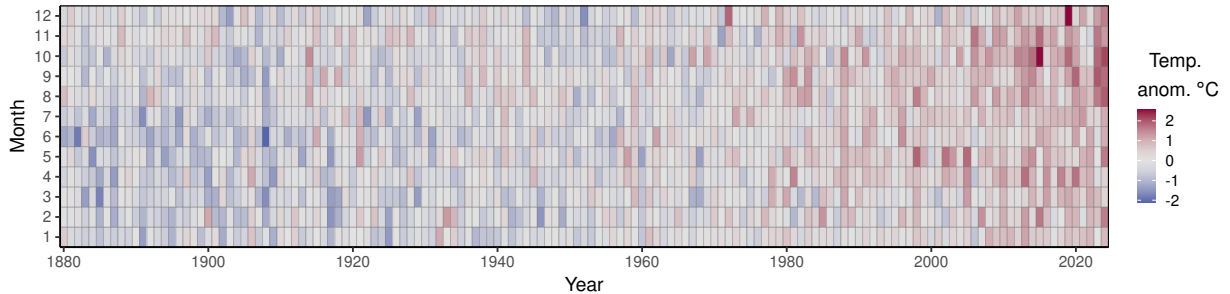


Figure 2: Heat map for non-geospatial gridded data. Year-monthly surface temperature anomaly time series in Western Australia, with continuous diverging colour scale.

This manuscript is organised as follows. In Section 2, we define rigorously density contour levels, and introduce our proposed approximation of density contour levels for gridded data. In Section 3, we verify the efficacy of this approximation for synthetic and experimental gridded data, as well as the increased interpretability of density contour levels over existing contour level selections methods. We end with some concluding remarks.

2 Density contours

We begin by examining the special case for a probability density function. A τ -density contour R_τ is defined as the smallest region that contains the upper τ probability of the density function f

$$R_\tau \equiv R_\tau(f) = \{\mathbf{x} : f(\mathbf{x}) \geq f_\tau\} \text{ and } \mathbb{P}(\mathbf{X} \in R_\tau) = \tau \quad (1)$$

where the random variable \mathbf{X} is drawn from f (Bowman and Foster, 1993; Hyndman, 1996). This definition of R_τ in Equation (1) involves the implicitly defined τ -density contour level f_τ . Hyndman (1996) asserts an alternative explicit definition of f_τ as the $(1 - \tau)$ -quantile of $Y = f(\mathbf{X})$, i.e.

$$f_\tau = F_Y^{-1}(1 - \tau) \quad (2)$$

where F_Y is the cumulative distribution function of Y . This quantile is well-defined as Y is a univariate random variable. Then, $\mathbb{P}(\mathbf{X} \in R_\tau) = \int_{\mathbb{R}^d} f(\mathbf{x}) \mathbf{1}\{f(\mathbf{x}) \geq f_\tau\} d\mathbf{x} = \mathbb{E}[\mathbf{1}\{f(\mathbf{X}) \geq f_\tau\}] = \mathbb{P}(f(\mathbf{X}) \geq f_\tau) = \mathbb{P}(Y \geq f_\tau) = 1 - F_Y(f_\tau) = 1 - F_Y(F_Y^{-1}(1 - \tau)) = \tau$, which verifies the probability associated with R_τ . The proof that R_τ has the minimal hypervolume amongst all sets of probability mass τ is more involved and the interested reader is urged to consult Hyndman (1996). We call R_τ a ‘density contour region’, following Polonik (1995); Chacón and Duong (2018), whilst Hyndman (1996) prefers ‘highest density region’. As an aside, we also note that τ is closely related to excess mass of R_τ (Polonik, 1995).

A set of m density contour levels $0 < \tau_1 < \dots < \tau_m < 1$, and their corresponding m density contour regions $R_{\tau_1}, \dots, R_{\tau_m}$, due to their probabilistic interpretations, facilitate an intuitive interpretation of density visualisations. Common choices include the quartile contours $\tau = 0.25, 0.5, 0.75$ or the odd decile contours $\tau = 0.1, 0.3, 0.5, 0.7, 0.9$, or the decile contours

$\tau = 0.1, \dots, 0.9$, depending the intricacy of structure of the density f . The upper limit of a suitable number of contour levels is most likely about eight since this approaches the limit of human abilities for visual differentiation (Jenks, 1963; Delicado and Vieu, 2015).

In Figure 3, we illustrate the added interpretability of density contour levels over a continuous colour scale for a multimodal Gaussian mixture density $3/11N((-1, 1), 1/8[1, 0; 0, 1]) + 4/11N((0, 0), 1/8[1, 9/10; 9/10, 1]) + 3/11N((1, -1), 1/8[1, 0; 0, 1])$. On the left is the heat map of the density function with a continuous colour scale, from ranging red (high density) to orange (mid) to yellow (low). Whilst we are able to ascertain some qualitative characteristics, such as the multimodality and the relative heights/locations of the modes, it is not straightforward to make more precise assertions. On the right, the solid black curves are the decile contours of the contour levels $f_{0.9} = 0.066, f_{0.7} = 0.183, f_{0.5} = 0.289, f_{0.3} = 0.379, f_{0.1} = 0.511$. The 10% contour region $R_{0.1}$ (red) is a connected region, whilst the 30% contour region $R_{0.3}$ (orange) is a disconnected region. The 30% contour region $R_{0.3}$ is the union of the red and orange regions, with the red region comprising 0.10 probability, and the orange region 0.2 probability. Analogously, the 90% contour region $R_{0.9}$ is the union of all the coloured regions. Since density contours can be disconnected regions, they allow for flexible interpretations of density functions.

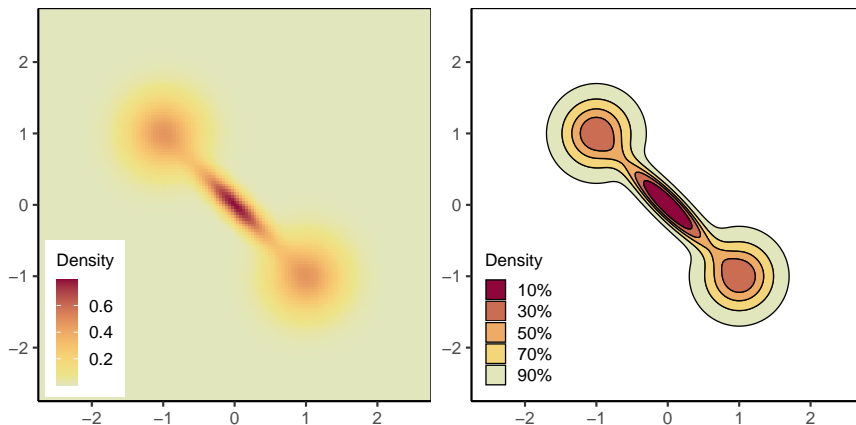


Figure 3: Gaussian mixture density $3/11N((-1, 1), 1/8[1, 0; 0, 1]) + 4/11N((0, 0), 1/8[1, 9/10; 9/10, 1]) + 3/11N((1, -1), 1/8[1, 0; 0, 1])$. (Left) Heat map with continuous colour scale, red (high) to orange (mid) to yellow (low). (Right) Decile 10%, 30%, 50%, 70%, 90% contour regions.

The density contour level f_τ in Equation (2) remains difficult to compute since it requires a closed form of both the density f and the cumulative distribution of $f(\mathbf{X})$. The mostly commonly deployed method is a quantile-based approximation from a random sample $\mathbf{X}_1, \dots, \mathbf{X}_n$ drawn from the common density f (Hyndman, 1996). From this sample data, we construct an estimator \hat{f} of the target density f . Within a parametric framework, maximum likelihood estimators are popular, and within a non-parametric framework, histograms and kernel density estimators are widely used. The estimation methodology does not need to be specified here as the following apply for any consistent density estimator. The τ -density contour level f_τ is consistently estimated by plug-in estimators of Equations (1–2), i.e., \hat{f}_τ is the sample $(1 - \tau)$ -quantile of $\hat{f}(\mathbf{X}_1), \dots, \hat{f}(\mathbf{X}_n)$. This approach is outlined in Algorithm 1. The inputs are the random sample of size n and the probability τ . The output is the approximate τ -density contour level \hat{f}_τ . In Step 1, we draw a random data sample $\mathbf{X}_1, \dots, \mathbf{X}_n$ of size n from the common density f . In Step 2, we compute the density estimate \hat{f} from the data sample. In Step 3, we compute the transformed data sample by evaluating the density estimate at the data sample values. In Step 4, the density contour level is approximated as the $(1 - \tau)$ -quantile of these transformed data values.

The calculations in Algorithm 1 are intuitive, efficient, and valid for any data dimension d

Algorithm 1 Quantile-based approximation of density contour level

Input: random sample $\mathbf{X}_1, \dots, \mathbf{X}_n$, n sample size, τ probability

Output: \hat{f}_τ approximate density contour level

- 1: Compute density estimate \hat{f} from $\mathbf{X}_1, \dots, \mathbf{X}_n$
 - 2: Evaluate density estimate at data sample values $\hat{f}(\mathbf{X}_1), \dots, \hat{f}(\mathbf{X}_n)$
 - 3: Approximate density contour level $\hat{f}_\tau := (1 - \tau)$ -quantile of $\hat{f}(\mathbf{X}_1), \dots, \hat{f}(\mathbf{X}_n)$
-

and any consistent density estimator \hat{f} , which has contributed to its wide acceptance. However we cannot employ this algorithm for our gridded data set since it requires direct access to the original point data sample. So we search for alternatives to Steps 2–3 which avoid explicit computations with the point data $\mathbf{X}_1, \dots, \mathbf{X}_n$.

For our proposed alternative in Algorithm 2, the inputs are the density estimate \hat{f} , a set of M grid points $G = \{\mathbf{g}_1, \dots, \mathbf{g}_M\}$, and the probability τ . In Step 1, we compute the hypervolume δ of a grid cell from G . In Steps 2–4, we compute the M probability elements for the grid G : the j th probability element p_j is obtained by multiplying the hypervolume δ and the density estimate value $\hat{f}(\mathbf{g}_j)$ at the grid point \mathbf{g}_j . In Steps 5–6, we compute the order statistics of the M probability elements, and their partial sums. In Step 7, we search for the smallest cell index j^* such that the partial sum is greater than or equal to $1 - \tau$, i.e. $P_{j^*} = p_{(j^*)} + \dots + p_{(M)}$ exceeds $1 - \tau$ by the least amount. By construction, the union $\tilde{R}_\tau = \mathbf{g}_{(j^*)} \cup \dots \cup \mathbf{g}_{(M)}$ is the smallest region, comprised of the grid cells, with probability mass $\geq (1 - \tau)$, i.e. \tilde{R}_τ is an approximation of R_τ . In Step 8, the density contour level is approximated by $\hat{f}(\mathbf{g}_{j^*})$.

Algorithm 2 Grid-based approximation of density contour level

Input: \hat{f} density estimate, G estimation grid, τ probability

Output: \hat{f}_τ approximate density contour level

- 1: Compute hypervolume of grid cell δ
 - 2: **for** $j := 1$ to M **do**
 - 3: Evaluate density estimate at grid point $\hat{f}(\mathbf{g}_j)$
 - 4: Compute probability element $p_j := \delta \hat{f}(\mathbf{g}_j)$
 - 5: Compute order statistics $p_{(1)} \leq \dots \leq p_{(M)}$ of probability elements
 - 6: Compute partial sums $P_j := \sum_{\ell=j}^M p_{(\ell)}$ of order statistics
 - 7: Find minimizer $j^* := \operatorname{argmin}_{j \in \{1, \dots, M\}} \{P_j \geq 1 - \tau\}$
 - 8: Approximate density contour level $\hat{f}_\tau := \hat{f}(\mathbf{g}_{j^*})$
-

Due to the invariance of density contour levels, Algorithm 2 can be adapted to any non-negative function g with a finite integral over the grid G . With \hat{g} , a grid-based estimate of g , we calculate S which is the sum of all probability elements of \hat{g} on the grid G . If we normalise the grid-based values as $\hat{f} = \hat{g}/S$, then \hat{f} is a suitable density estimate input in Algorithm 2. Since the order statistics of $p_1/S, \dots, p_M/S$ remain the same as those for p_1, \dots, p_M , then the approximate contour level for g is $\tilde{g}_\tau = S \hat{f}_\tau$. Since f, \hat{f} are bona fide probability densities, then a probabilistic interpretation applies to $\{\mathbf{x} : \hat{g}(\mathbf{x}) \geq \tilde{g}_\tau\}$ similar to $\tilde{R}_\tau = \{\mathbf{x} : \hat{f}(\mathbf{x}) \geq \hat{f}_\tau\}$. This is the situation for the Paris population data.

Furthermore, for a function g whose range includes negative and positive values, then we partition $g = g^+ - g^-$, where $g^-(\mathbf{x}) = -\mathbf{1}\{g(\mathbf{x}) \leq 0\}g(\mathbf{x})$ and $g^+(\mathbf{x}) = \mathbf{1}\{g(\mathbf{x}) > 0\}g(\mathbf{x})$, where $\mathbf{1}\{\cdot\}$ is the indicator function. Since g^-, g^+ are non-negative functions, then we can apply Algorithm 2 to each of them, resulting in contour levels $\tilde{g}_\tau^-, \tilde{g}_\tau^+$ for each of the negative and positive values of g , yielding the contour regions $\{\mathbf{x} : \hat{g}(\mathbf{x}) \leq \tilde{g}_\tau^-\}$ and $\{\mathbf{x} : \hat{g}(\mathbf{x}) \geq \tilde{g}_\tau^+\}$ respectively. Whilst g, \hat{g} cannot be associated with any bona fide densities, and so these contour regions do not have a probabilistic interpretation, $\tilde{g}_\tau^-, \tilde{g}_\tau^+$ remain suitable contour level choices

for visualising \hat{g} . Thus Algorithm 2 can be adapted to compute contour levels for any grid-based real-valued function, and is not restricted to density functions. This is the situation for the temperature anomaly data.

We conclude with a brief description of several other contour level selection methods. The naive quantile contour levels compute the τ -quantile of all values in the grid $\hat{f}(\mathbf{g}_1), \dots, \hat{f}(\mathbf{g}_M)$. Suppose that we select m naive quantile contour levels, then for comparison, we can compute the m equal interval length contour levels, namely $\hat{f}_{\min} + k/m \cdot (\hat{f}_{\max} - \hat{f}_{\min}), j = 1, \dots, m$, or the m ‘natural’ or Jenks contour levels (Jenks, 1967), which is a k -means clustering with m clusters of $\hat{f}(\mathbf{g}_1), \dots, \hat{f}(\mathbf{g}_M)$. These contour level selection methods are easy to understand and to implement than the density contour levels, though the former lack the probabilistic interpretation of the latter. In the following section, we compare the empirical performance of these contour level selection methods to density contour levels for synthetic and experimental data.

3 Data analysis

To demonstrate the applicability of density contour levels for gridded data, we deploy the visualisation capabilities of the R statistical analysis environment. Due to the simplicity of Algorithm 2, it can be implemented in any visualisation software.

3.1 Synthetic data

We focus on three bivariate Gaussian mixture densities: Density #1 is a base case $N((-1, 0), [1/4, 0; 0, 1])$; Density #2 is bimodal with asymmetric modes $1/4N((-1, 0), [1/4, 0; 0, 1]) + 3/4N((1, 0), [1/4, 0; 0, 1])$; and Density #3 is trimodal with a central mode oriented obliquely from the coordinates axes $3/11N((-1, 1), 1/8[1, 0; 0, 1]) + 4/11N((0, 0), 1/8[1, 9/10; 9/10, 1]) + 3/11N((1, -1), 1/8[1, 0; 0, 1])$. For each density, we draw a Monte Carlo $N = 10^6$ random sample $\mathbf{X}_1, \dots, \mathbf{X}_N$, and we transform this random sample using the target Gaussian mixture density f to obtain $f(\mathbf{X}_1), \dots, f(\mathbf{X}_N)$. The quantile-based approximation f_τ^* is the upper τ -quantile of $f(\mathbf{X}_1), \dots, f(\mathbf{X}_N)$, from which we can establish $R_\tau^* = \{\mathbf{x} : f(\mathbf{x}) \geq f_\tau^*\}$. We use f_τ^*, R_τ^* as the proxies for f_τ, R_τ . These $R_\tau^*, \tau = 0.1, 0.3, 0.5, 0.7, 0.9$ are displayed as the density contour regions in the first row in Figure 4.

To mimic the situation where we have a data sample at hand, we draw an $n = 10000$ random sample from the target Gaussian mixture density, apply Algorithm 1 with a kernel density estimate \hat{f} , on an $M = 151 \times 151$ grid, to yield quantile-based estimates \hat{f}_τ and \hat{R}_τ . The kernel density estimate is computed using a plug-in bandwidth (Duong and Hazelton, 2003), though any sensible density estimate can be used here. These $\hat{R}_{0.1}, \dots, \hat{R}_{0.9}$ are the second row in Figure 4. To mimic the situation where we only have access to the gridded density estimate and we do not have access to the data sample, then we input only the grid of the previous kernel density estimate values $\hat{f}(\mathbf{g}_1), \dots, \hat{f}(\mathbf{g}_M)$ into Algorithm 2 to yield the grid-based approximations \tilde{f}_τ and \tilde{R}_τ . The approximation computations are carried out by the `as.kde` function in the `ks` package (Duong, 2005) or by the `tidy_as_kde/st_as_kde` functions in the `eks` package (Duong, 2022). These $\tilde{R}_{0.1}, \dots, \tilde{R}_{0.9}$ are the third row in Figure 4. We observe that the contour region estimates $\hat{R}_\tau, \tilde{R}_\tau$ generally remain close to R_τ^* , and the differences between the quantile-based \hat{R}_τ and the grid-based \tilde{R}_τ approximations tend to be small. This gives us confidence that the grid-based contour levels in Algorithm 2 are as accurate as their widely accepted quantile-based counterparts.

To supplement the visual inspection in Figure 4, we repeat the above computations for 100 replicates for $n = 1000$ and 10000. For each replicate, we draw random sample of size n from the target Gaussian mixture density, apply Algorithm 1 with a kernel density estimate \hat{f} , on an $M = 151 \times 151$ grid G , to yield quantile-based estimates \hat{f}_τ and \hat{R}_τ . Then we input only the

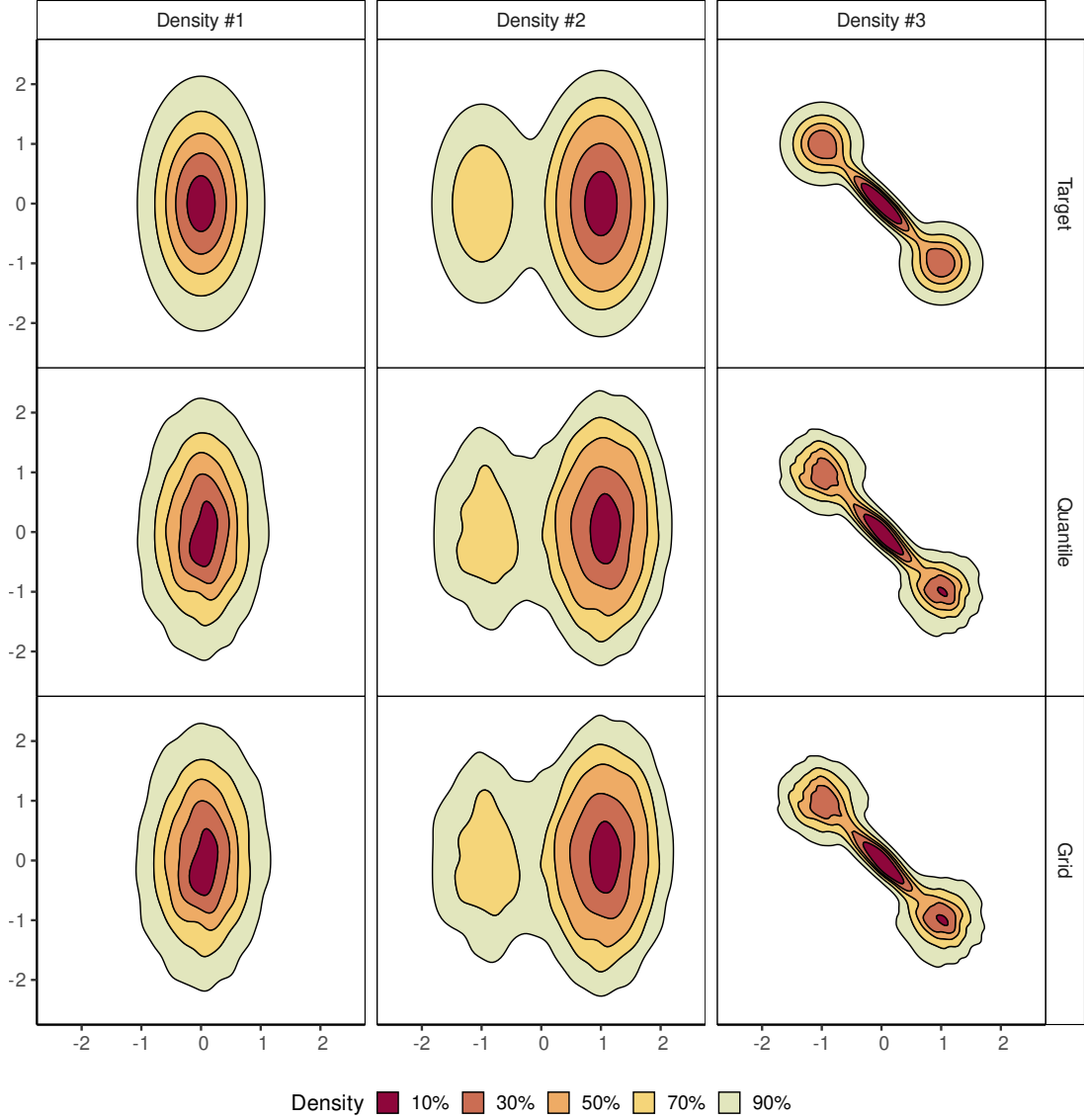


Figure 4: Density contour approximations for bivariate Gaussian mixture densities, $\tau = 0.1, 0.3, 0.5, 0.7, 0.9$. (Left) Density #1 unimodal. (Centre) Density #2 bimodal. (Right) Density #3 trimodal. (First row) Target density contour regions R_τ^* . (Second row) Quantile-based approximate contour regions \hat{R}_τ . (Third row) Grid-based approximate contour regions \tilde{R}_τ . Approximations are based on $n = 10000$ sample and 151×151 grid.

grid of the previous kernel density estimate values $\hat{f}(\mathbf{g}_1), \dots, \hat{f}(\mathbf{g}_M)$ into Algorithm 2 to yield the grid-based approximations \tilde{f}_τ and \tilde{R}_τ . The performance of the contour level estimates $\hat{f}_\tau, \tilde{f}_\tau$ is not the primary quantity of interest, but rather it is the performance of the contour region estimates $\hat{R}_\tau, \tilde{R}_\tau$. So we compute $\text{Err}(\hat{R}_\tau) = \mathbb{P}(\mathbf{X} \in \hat{R}_\tau \Delta R_\tau)$ and $\text{Err}(\tilde{R}_\tau) = \mathbb{P}(\mathbf{X} \in \tilde{R}_\tau \Delta R_\tau)$, where $A \Delta B = A \cup B \setminus (A \cap B)$ is the symmetric difference between sets A, B . These probabilities are approximated as Riemann sums.

The box plots of these errors for $\tau = 0.1, 0.3, 0.5, 0.7, 0.9$ are displayed in Figure 5. Each column is for each target density. The upper row is for the sample size $n = 1000$, and the lower row for $n = 10000$. The vertical axis is the contour upper probability τ , the horizontal axis is the contour region estimate error. For each τ , the box plot for quantile-based approximation is in white and for the grid-based approximation is in grey. The most important conclusion from these box plots is that the increase in the contour region region estimation error for a grid-based approximation \tilde{R}_τ over its quantile-based approximation \hat{R}_τ is small, especially for the larger

sample size $n = 10000$. For small $\tau = 0.1$, $\text{Err}(\hat{R}_{0.1}), \text{Err}(\tilde{R}_{0.1})$ are also small, whilst the area of $R_{0.1}$ is small. The boundary of the contour region $R_{0.1}$ has high density values, so there is a large jump in the evaluations of the density estimate at the observations/grid cells just outside of this boundary which tends to ensure that they correctly contribute to estimates of the lower density contour regions $\tau > 0.1$ and so $\text{Err}(\hat{R}_{0.1}), \text{Err}(\tilde{R}_{0.1})$ remain small. For large $\tau = 0.9$, the boundary of the contour region $R_{0.9}$ has low density values close to zero. So small differences in $\tilde{f}_{0.9}$ to $f_{0.9}$ may lead to relatively larger values in $\text{Err}(\tilde{R}_{0.9})$ than $\text{Err}(\hat{R}_{0.9})$.

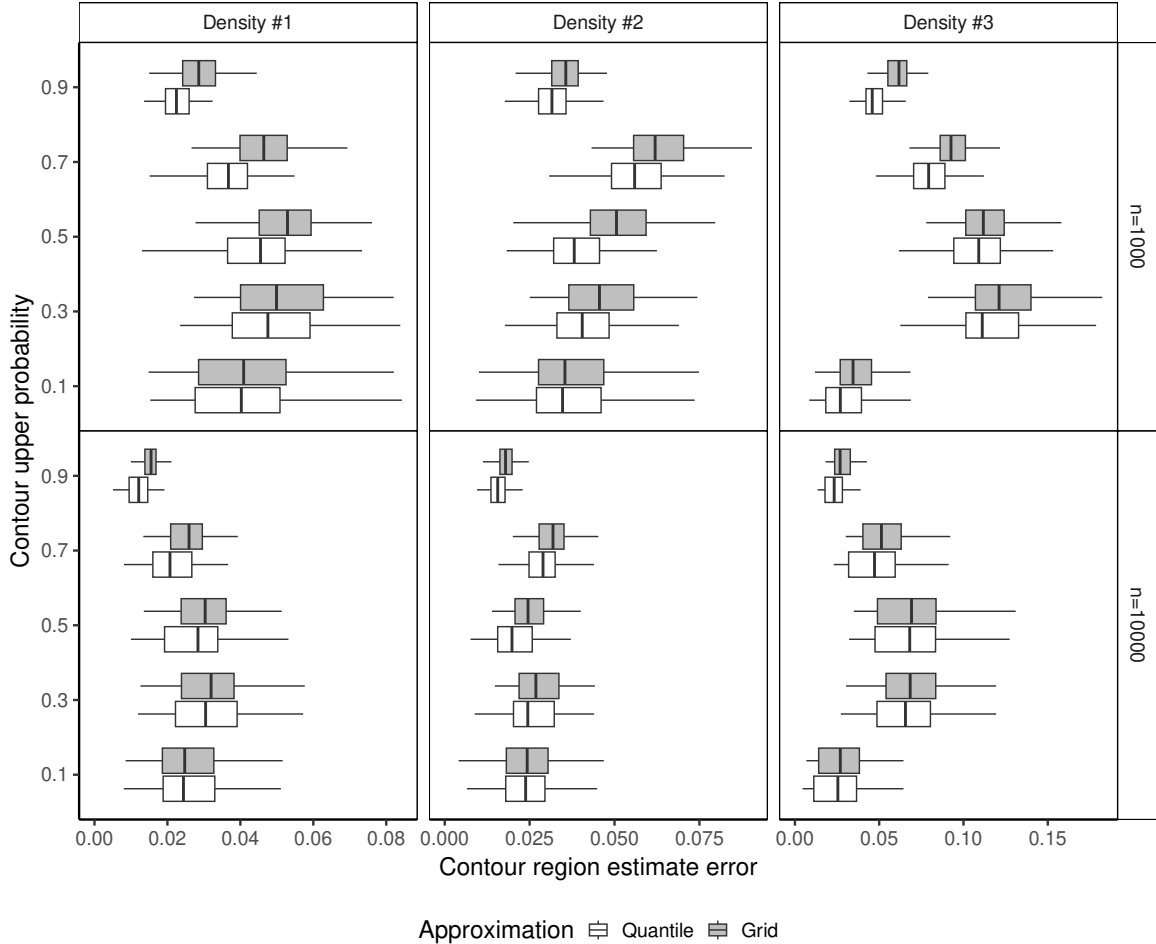


Figure 5: Errors of quantile- and grid-based estimates of contour regions of normal mixture densities, for $\tau = 0.1, 0.3, 0.5, 0.7, 0.9$. Each column is each target density. Upper row is sample size $n = 1000$, lower row is $n = 10000$. Vertical axis is contour probability τ , horizontal axis is contour region estimate error. Box plots: quantile-based (white), grid-based (grey).

Figure 5 is solid evidence of the accuracy of the grid-based approximation of density contour levels with respect to the widely accepted quantile-based approximation, so we move on to comparing them to the other contour level selection methods. This comparison is more subjective as there is no single, widely accepted quantitative comparison. In Figure 6, for each gridded density estimate on a 151×151 grid computed from a single $n = 10000$ sample drawn from each Gaussian mixture: the first row is the density estimate with density contour levels, the second with equal length intervals, the third with naive quantiles, and the fourth with natural contour levels. Since all these three Gaussian mixture modals have similar general comparisons, we focus on Density #3.

The density contour levels are $\tilde{f}_{0.9} = 0.061, \tilde{f}_{0.7} = 0.171, \tilde{f}_{0.5} = 0.268, \tilde{f}_{0.3} = 0.345, \tilde{f}_{0.1} = 0.445$, and they describe the multimodality structure well. The equal length intervals are $0.113, 0.227, 0.340, 0.454, 0.567$, which are similar to the density contour levels: they highlight

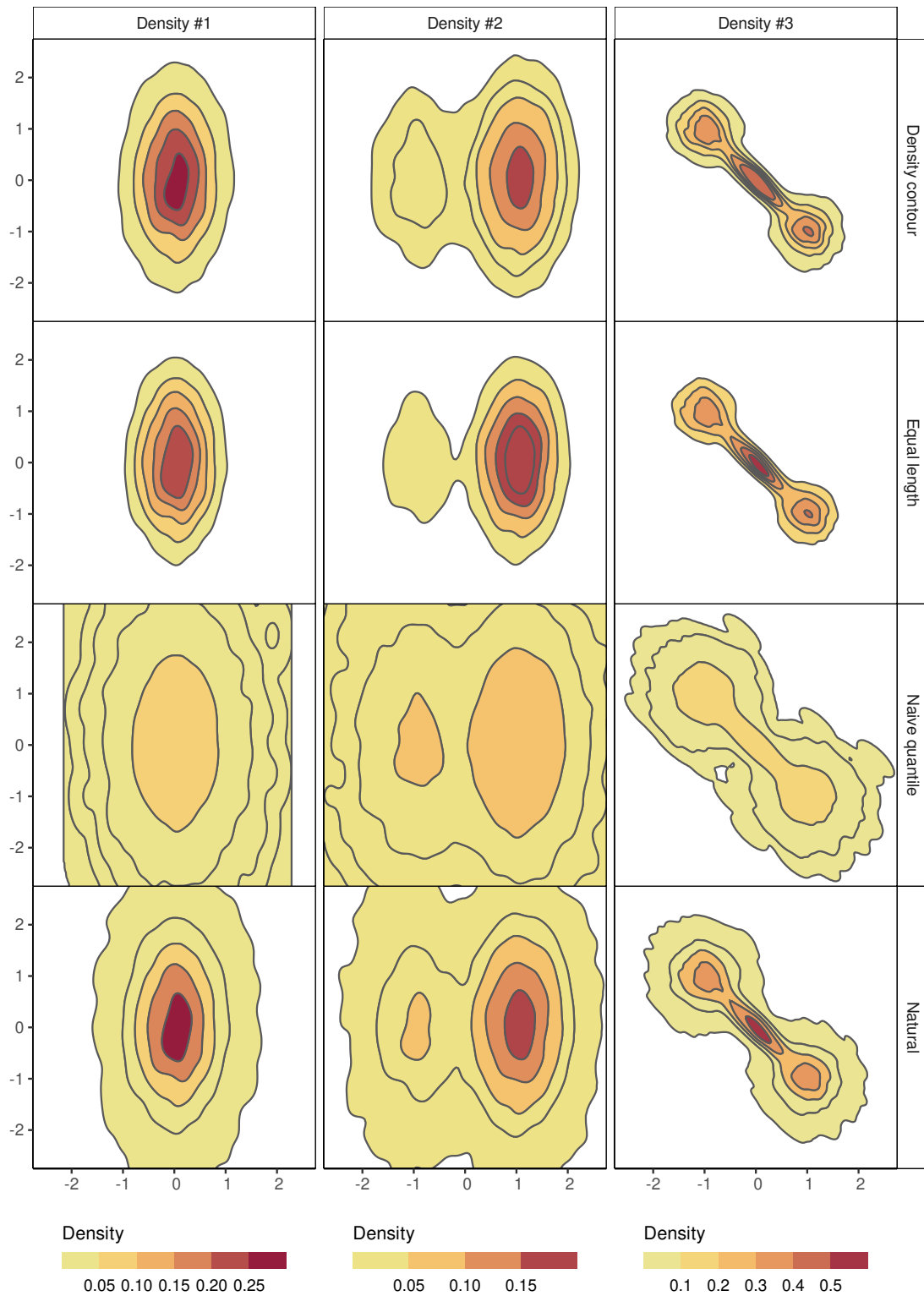


Figure 6: Comparison of contour level selection methods for gridded density estimates from Gaussian mixture densities. (First row) Density contour. (Second row) Equal length. (Third row) Naive quantile. (Fourth row) Natural (Jenks). Density estimates based on $n = 10\,000$ sample.

better the peaked middle mode, but less well the smaller modes. The naive quantile contour levels are 0.00000, 0.00001, 0.0043, 0.130. As the vast majority of the gridded estimate values are close to zero, then these naive quantile levels are heavily skewed towards zero, and the

contour plot at these levels does not reveal any multimodality. The natural contour levels are 0.003, 0.085, 0.203, 0.338, 0.518, which produces a good overall contour plot, though it suffers in comparison to the density contour levels upon closer inspection, since the former show the middle mode to be taller but occupies less area, and the outer modes to be noisier and with heavier tails.

3.2 Experimental data

For our analysis of experimental data, we return to the gridded data from Figure 1. For the Paris population data, there are 2078 1×1 km square polygons in the Lambert Azimuthal Equal Area Europe (EPSG 3035) projected coordinates system. For the southern Indo-Pacific surface temperature anomaly data, the 970 $2^\circ \times 2^\circ$ square polygons are transformed to curvilinear polygons in the Australian Albers projection (EPSG 9473). Since we rely on software which requires density estimates on uniform rectilinear grids aligned to the coordinate axes, these polygon grids require some pre-processing. That is, we interpolate them to a uniform rectangular grid which is aligned to the coordinate axes. For the population data, the result is $M = 57 \times 43 = 2451$ grid cells (1×1 km) covering $[3.735e6, 3.792e6] \times [2.867e6, 2.910e6]$, and for the temperature anomaly data, $M = 36 \times 27 = 972$ grid cells (200×200 km, which is approximately equal to $2^\circ \times 2^\circ$ since $1^\circ \approx 111$ km at the Equator) covering $[-4.5e6, 2.7e6] \times [-5.4e6, 0]$. The interpolated gridded data $\hat{f}(g_1), \dots, \hat{f}(g_M)$ are displayed in Figure 7.

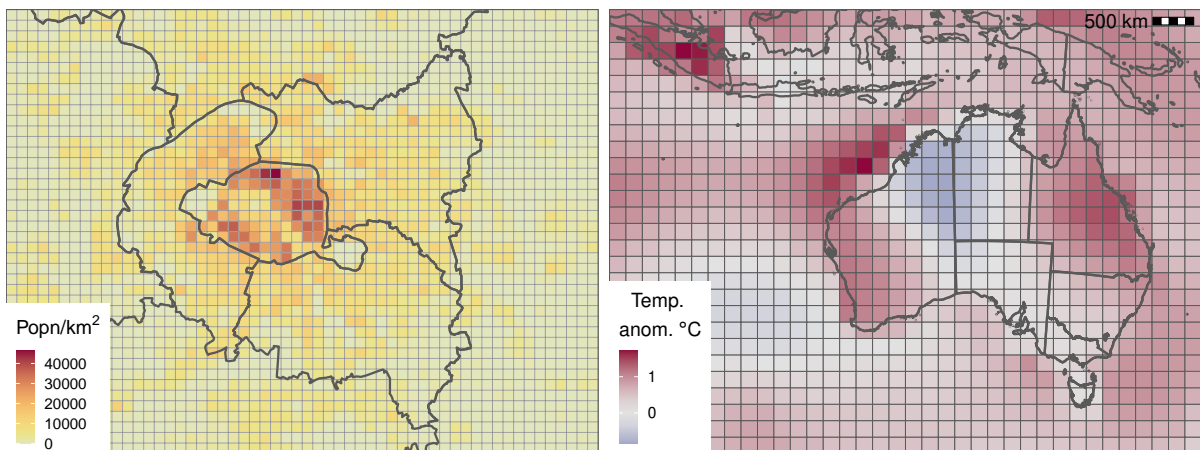


Figure 7: Interpolated gridded data. (Left) Population of Paris city region on 1×1 km grid, with continuous sequential colour scale. (Right) Temperature anomaly in southern Indo-Pacific region on 200×200 km grid, with continuous diverging colour scale.

In Figure 8(a) are the contour regions of the Paris population interpolated gridded data corresponding to the density contour levels: $\tilde{f}_{0.1} = 30\,237$ (red), $\tilde{f}_{0.3} = 15\,288$ (dark orange), $\tilde{f}_{0.5} = 9\,606$ (mid orange), $\tilde{f}_{0.7} = 6\,410$ (light orange), $\tilde{f}_{0.9} = 3\,186$ (yellow). The red region is $\tilde{R}_{0.1} = \{x : \hat{f}(x) \geq \tilde{f}_{0.1}\}$ etc. In comparison to the continuous colour scale, these contour regions provide a more interpretable visualisation of the population distribution. The population hotspots can be more quantitatively defined as, say, the 10% density contour region $\tilde{R}_{0.1}$. That is, we can consider any area with population density of at least 30 237 per km^2 to be densely populated with respect to the rest of the ROI. The area of $\tilde{R}_{0.1}$ is 22.29 km^2 , which is 0.91% of the total ROI area of 2451 km^2 . Whereas the population in $\tilde{R}_{0.1}$ is 957 473.5 which is 10.09% of the total ROI population of 9 490 878. In addition, we can consider any grid cell with population density less than the 90% density contour level $\tilde{f}_{0.9} = 3\,186$ per km^2 to be sparsely populated. The area of $\tilde{R}_{0.9}$ is 921.80 km^2 , which is 37.61% of the total area of the ROI, whilst it comprises 8 513 908 people (89.71% of the ROI population). These contour regions quantify the highly unequal population spatial distribution in the ROI.

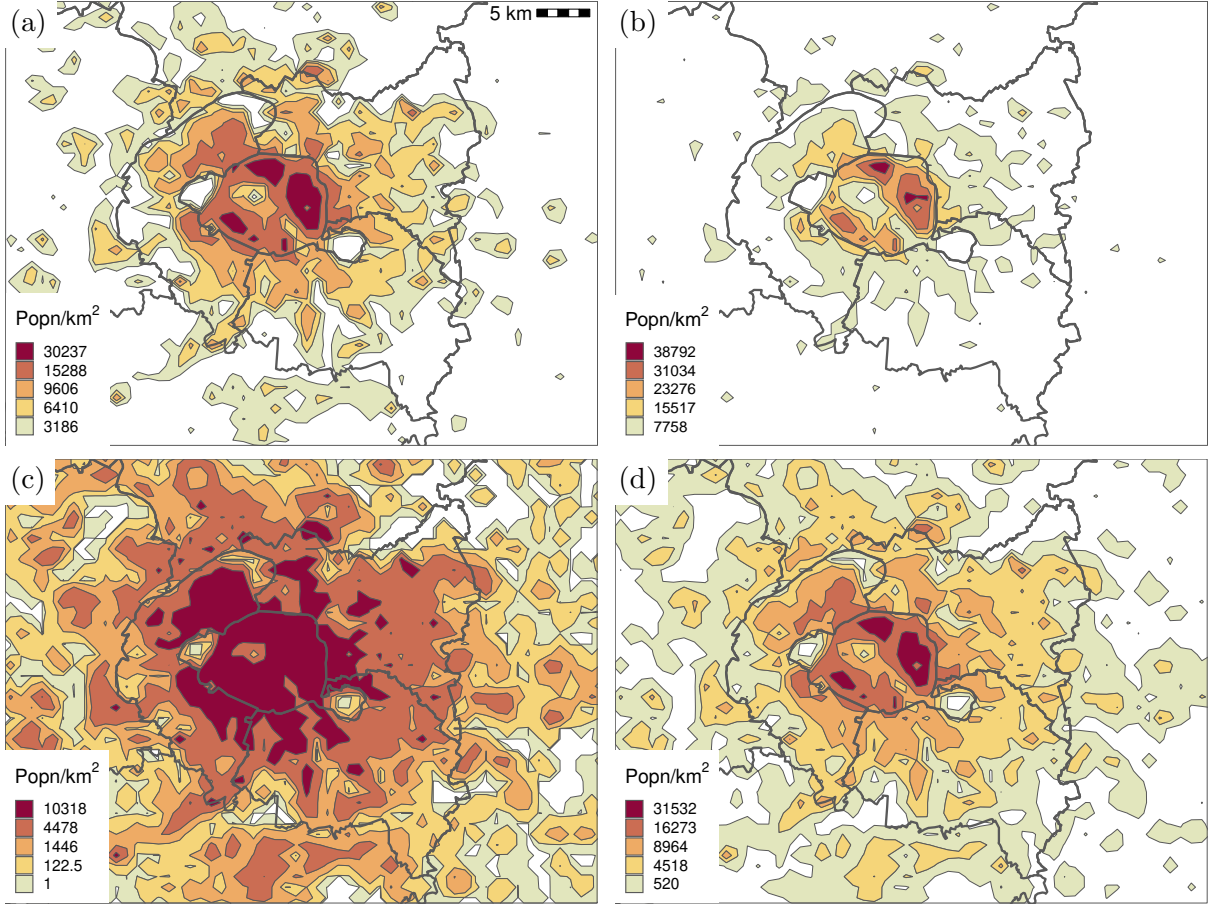


Figure 8: Contour regions for population density for Paris capital region on 1×1 km grid. (a) Density contour levels: red (10%) to orange (50%) to yellow (90%). (b) Equal length contour levels. (c) Naive quantile contour levels. (d) Natural (Jenks) contour levels.

The equal length contour intervals are 38 792 (red), 31 034 (dark orange), 23 276 (mid orange), 15 517 (light orange), 7 758 (yellow) in Figure 8(b). These contour levels emphasise the higher population densities: the higher levels delimit well the hotspots, but the lower levels do not delimit the domain of the spatial population distribution as well as the 90% density contour. The naive quantile contour levels are 10 318 (red), 4 478 (dark orange), 1 446 (mid orange), 122 (light orange), 1 (yellow) in Figure 8(c). Since zero or low population densities are by far the most numerous, these contour levels give the erroneous impression that the population distribution is more evenly spread throughout the ROI. The natural contour levels 31 532 (red), 16 273 (dark orange), 8 964 (mid orange), 4 518 (light orange), 520 (yellow) in Figure 8(d) reveal a similar contour plot with density contour levels, though the lower levels give the visual impression that the population distribution is more evenly spread in the peripheral areas of the ROI.

The contour plots for the southern Indo-Pacific surface temperature anomaly interpolated gridded data are shown in Figure 9. Since these temperature anomalies can be negative or positive, then we compute the quartile density contour levels \tilde{f}_τ , $\tau = 0.25, 0.5, 0.75$ for each set of negative- and positive-valued grid cells, namely $\leq -0.69^\circ\text{C}$ (dark blue), $\leq -0.44^\circ\text{C}$ (mid blue), $\leq -0.26^\circ\text{C}$ (light blue) and $\geq 0.57^\circ\text{C}$ (light red), $\geq 0.79^\circ\text{C}$ (mid red), $\geq 1.00^\circ\text{C}$ (dark red). We interpret the dark blue region as $\{\mathbf{x} : \hat{f}(\mathbf{x}) \leq -0.69^\circ\text{C}\}$, the dark red region as $\{\mathbf{x} : \hat{f}(\mathbf{x}) \geq 1.00^\circ\text{C}\}$, and the light grey region as $\{\mathbf{x} : 0.44^\circ\text{C} \geq \hat{f}(\mathbf{x}) \geq -0.26^\circ\text{C}\}$ etc. Setting these contour density contour levels for negative and positive values separately yields a contour plot that covers the different anomaly ranges well in Figure 9(a). For the equal length contour levels, there are 2 negative and 4 positive contour levels, so they emphasise the hot anomalies in

Figure 9(b). The naive contour levels do not reach the extremities of the density contour levels, so the dark red/blue regions in Figure 9(c) give an erroneous impression that the anomalies are more widespread. The natural contour levels are similar to the density contour levels, though Figure 9(d) emphasises less the hot anomalies off the western and eastern coastal regions of Australia.

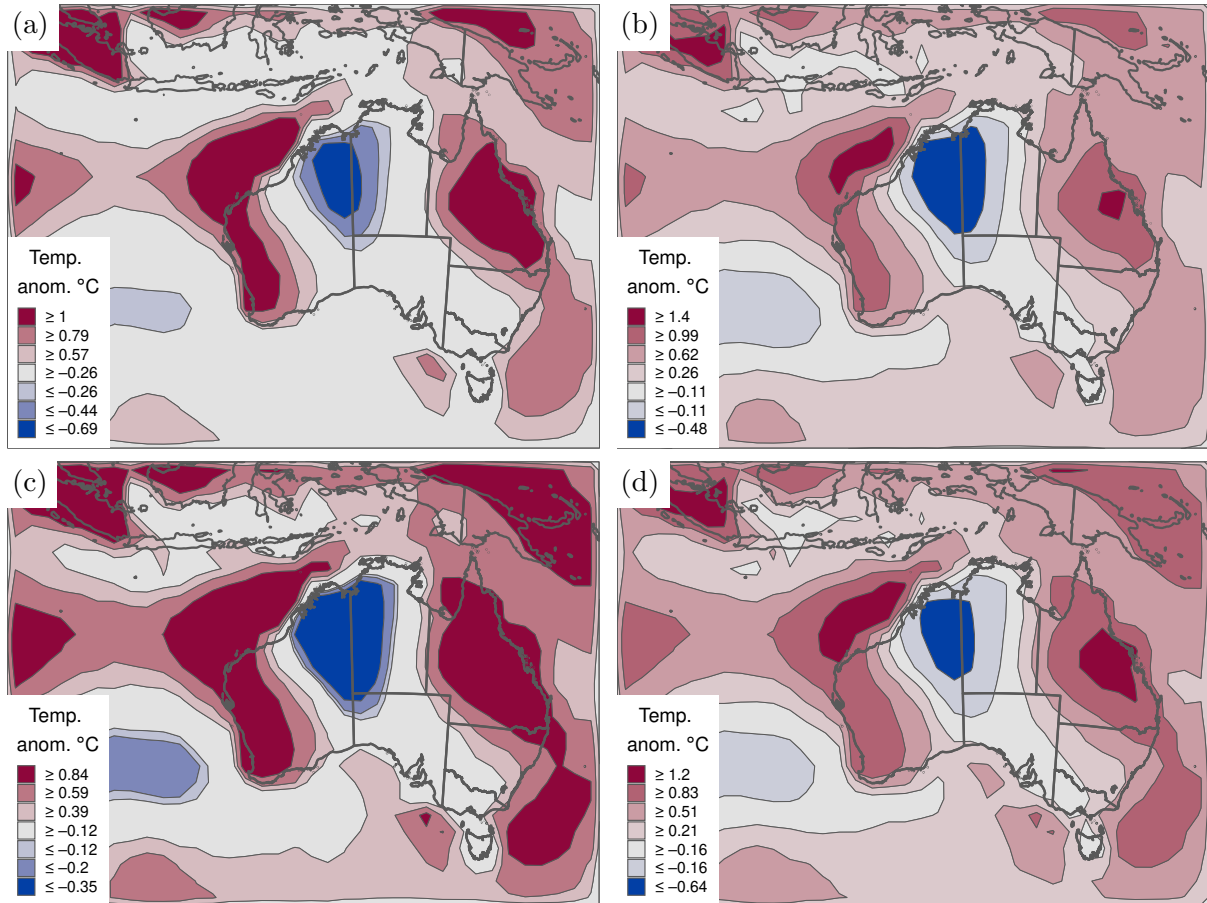


Figure 9: Contour regions for temperature anomalies for southern Indo-Pacific region on 200×200 km grid. (a) Density contour levels. (b) Equal length contour levels. (c) Naive quantile contour levels. (d) Natural (Jenks) contour levels

For the year-monthly temperature anomaly times series in Western Australia, we are able to compute the analogous contour levels. Since these are non-spatial gridded data, we do not compute contour regions as above and instead we visualise the time series heat maps with the reduced number of colours corresponding to the contour levels. In the first row in Figure 10 are the quartile density contour levels, $\tau = 0.25, 0.5, 0.75$. There is a large interval of anomalies in $[-0.73^\circ\text{C}, 0.77^\circ\text{C}]$ that are considered to be neutral (grey), so the warming trends (above 1.2°C in dark red) since the 2000s and in the second half of the year become more prominent. The equal length contour levels (second row) gives the impression of more gradual warming trends since most grid cells are coloured in light blue, grey or light red. On the other hand, in the naive quartile contour levels (third row), most grid cells are coloured in mid/dark blue or mid/dark red, which over-emphasise the warming trends. The natural contour levels (fourth row) is the most similar to the density contour levels, though the warming trends are less prominent due to the larger number of mid blue/mid red grid cells spread more evenly through the time series heat map.

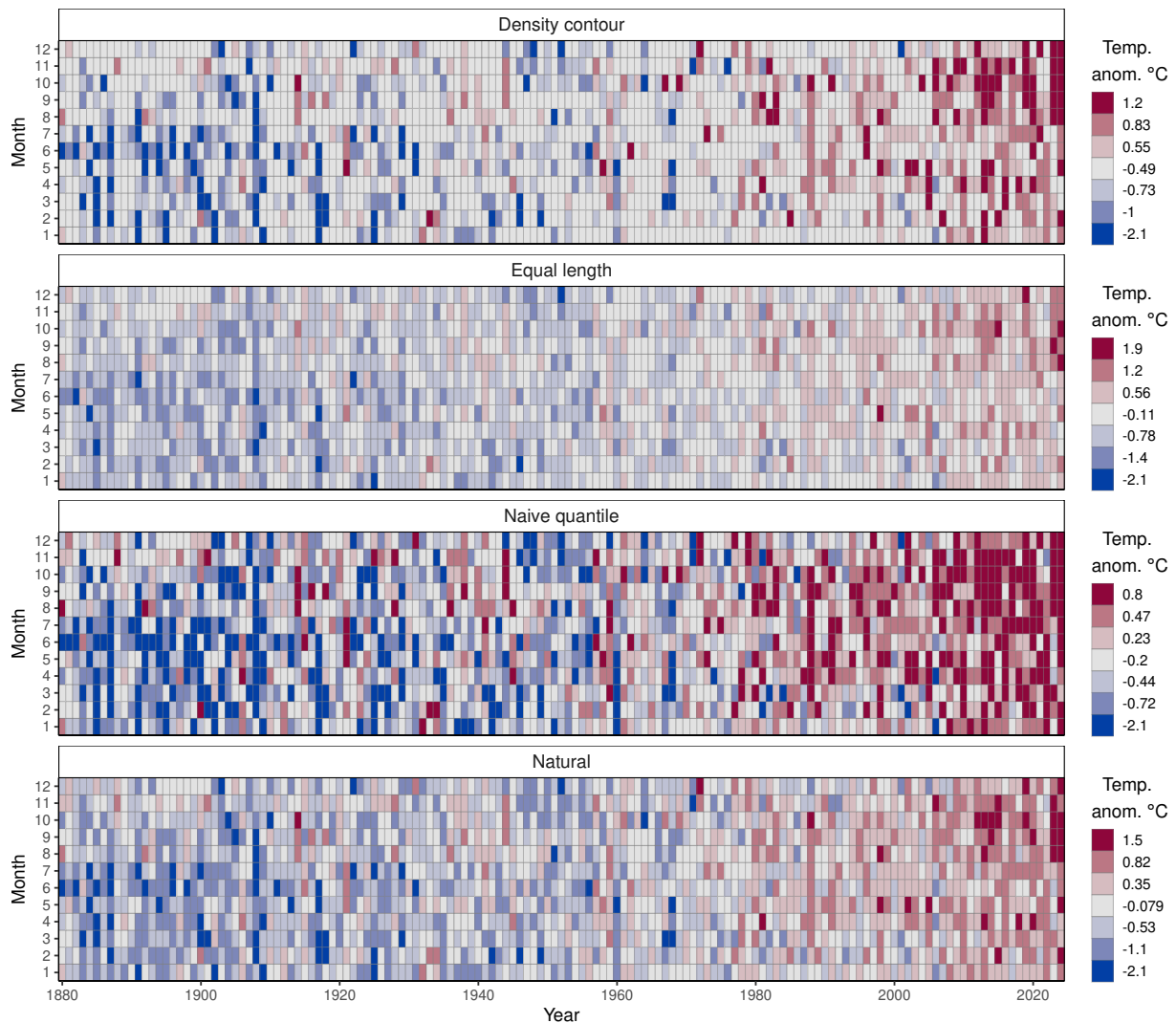


Figure 10: Heat maps for year-monthly temperature anomaly time series in Western Australia. (First row) Density contour levels. (Second) Equal length contour levels. (Third) Naive quantile contour levels. (Fourth) Natural (Jenks) contour levels.

4 Conclusion

Gridded data are an important data format for the dissemination and storage of open data. Density contour levels are widely deployed to create interpretable visualisations, and so we have introduced algorithms to compute density contour levels for any type of numerical gridded data. We demonstrated that for synthetic and experimental gridded data, our proposal leads to more interpretable visualisations than the current contour level selection methods. In addition to their visualisation properties, the rigorous probabilistic properties of density contour levels form the basis for further quantitative analyses, such as hotspot and home range analysis. These algorithms are available in R packages on the official CRAN repository to facilitate their wider deployment for statistical data analysis.

References

Baíllo, A. and J. E. Chacón (2021). Chapter 1 - statistical outline of animal home ranges: An application of set estimation. In A. S. R. Srinivasa Rao and C. R. Rao (Eds.), *Data Science: Theory and Applications*, Volume 44 of *Handbook of Statistics*, pp. 3–37. Elsevier.

- Bowman, A. W. and P. Foster (1993). Adaptive smoothing and density-based tests of multivariate normality. *Journal of the American Statistical Association* 88, 529–537.
- Chacón, J. E. and T. Duong (2018). *Multivariate Kernel Smoothing and Its Applications*. Boca Raton: Chapman and Hall/CRC.
- Delicado, P. and P. Vieu (2015). Optimal level sets for bivariate density representation. *Journal of Multivariate Analysis* 140, 1–18.
- Dobson, M. W. (1973). Choropleth maps without class intervals?: A comment. *Geographical Analysis* 5, 358–360.
- Duong, T. (2005). *ks: Kernel Smoothing*. R package version 1.15.0.
- Duong, T. (2022). *eks: Tidy and Geospatial Kernel Smoothing*. R package version 1.1.0.
- Duong, T. and M. L. Hazelton (2003). Plug-in bandwidth matrices for bivariate kernel density estimation. *Journal of Nonparametric Statistics* 15, 17–30.
- GISTEMP Team (2025). GISS surface temperature analysis (GISTEMP), version 4. <https://data.giss.nasa.gov/gistemp/>.
- Hyndman, R. J. (1996). Computing and graphing highest density regions. *American Statistician* 50, 120–126.
- Insee (2019). Revenus, pauvreté et niveau de vie en 2019 - données carroyées [In French]. <https://www.insee.fr/fr/statistiques/7655511?sommaire=7655515>.
- Jenks, G. F. (1963). Generalization in statistical mapping. *Annals of the Association of American Geographers* 53, 15–26.
- Jenks, G. F. (1967). The data model concept in statistical mapping. *International Yearbook of Cartography* 7, 186–190.
- Klemelä, J. (2009). *Smoothing of Multivariate Data: Density Estimation and Visualization*. New York: Wiley.
- Lenssen, N., G. A. Schmidt, M. Hendrickson, P. Jacobs, M. J. Menne, and R. Ruedy (2024). A NASA GISTEMPv4 observational uncertainty ensemble. *Journal of Geophysical Research: Atmospheres* 129, e2023JD040179.
- Polonik, W. (1995). Measuring mass concentrations and estimating density contour clusters – an excess mass approach. *Annals of Statistics* 23, 855–881.
- Schauer, K., T. Duong, K. Bleakley, S. Bardin, M. Bornens, and B. Goud (2010). Probabilistic density maps to study global endomembrane organization. *Nature Methods* 7, 560–568.
- Tobler, W. R. (1973). Choropleth maps without class intervals? *Geographical Analysis* 5, 262–265.
- Vose, R. S., B. Huang, X. Yin, D. Arndt, D. R. Easterling, J. H. Lawrimore, M. J. Menne, A. Sanchez-Lugo, and H. M. Zhang (2021). Implementing full spatial coverage in NOAA’s global temperature analysis. *Geophysical Research Letters* 48, e2020GL090873.
- Xie, Z. and J. Yan (2008). Kernel density estimation of traffic accidents in a network space. *Computers, Environment and Urban Systems* 32, 396–406.
- Zeileis, A., K. Hornik, and P. Murrell (2009). Escaping RGBland: Selecting colors for statistical graphics. *Computational Statistics and Data Analysis* 53, 3259–3270.